Water Science and Engineering 2017, 10(2): 143−153

HOSTED BY

ELSEVIER

CrossMark

Available online at www.sciencedirect.com

Water Science and Engineering

journal homepage: http://www.waterjournal.cn

Parametric study on smoothed particle hydrodynamics for accurate determination of drag coefficient for a circular cylinder

Maziar Gholami Korzani [a,*], Sergio A. Galindo-Torres [a,b], Alexander Scheuermann [a], David J. Williams [a]

[a] School of Civil Engineering, The University of Queensland, St Lucia, Brisbane, QLD 4072, Australia

[b] School of Mathematics and Physics, The University of Queensland, St Lucia, Brisbane, QLD 4072, Australia

Received 16 November 2016; accepted 21 March 2017

Available online 13 June 2017

Abstract

Simulations of two-dimensional (2D) flow past a circular cylinder with the smoothed particle hydrodynamics (SPH) method were conducted in order to accurately determine the drag coefficient. The fluid was modeled as a viscous liquid with weak compressibility. Boundary conditions, such as a no-slip solid wall, inflow and outflow, and periodic boundaries, were employed to resemble the physical problem. A sensitivity analysis, which has been rarely addressed in previous studies, was conducted on several SPH parameters. Hence, the effects of distinct parameters, such as the kernel choices and the domain dimensions, were investigated with the goal of obtaining highly accurate results. A range of Reynolds numbers (1−500) was simulated, and the results were compared with existing experimental data. It was observed that the domain dimensions and the resolution of SPH particles, in comparison to the obstacle size, affected the obtained drag coefficient significantly. Other parameters, such as the background pressure, influenced the transient condition, but did not influence the steady state at which the drag coefficient was determined.

Keywords: Smoothed particle hydrodynamics; Drag coefficient; Reynolds number; Sensitivity analysis; Viscous flow

1. Introduction

Recent advancements in high-performance computing technologies have had significant impacts on mesh-free methods such as smoothed particle hydrodynamics (SPH) in computational fluid dynamics (CFD). Although SPH is computationally expensive due to intensive interactions between integration points (in a misleading manner also denoted as particles), it may be advantageous in several situations, including moving boundaries (e.g., free-surface flow), complex boundary geometries, and shock wave simulations. Consequently, SPH has grown in popularity since its inception in 1977 for astrophysics purposes (Gingold and Monaghan, 1977; Lucy, 1977). Furthermore, recent developments in this method have extended its applicability to several engineering and scientific areas (Liu and Liu, 2005; Monaghan and Gingold, 1983) including fluid and solid dynamics (Gray et al., 2001), coastal management (Mirmohammadi and Ketabdari, 2011), and geotechnical engineering (Bui et al., 2007). In order to ensure the best performance, the accuracy, stability, and validity of SPH still need to be investigated thoroughly, since it is rather a new numerical approach.

Despite the growing popularity of SPH, there have been few studies on the sensitivity of results to SPH parameters and the influence of SPH variables on the accuracy of results. On the other hand, this method is better known for simulating

This work was supported by the Australian Research Council Discovery Project (Grant No. DP120102188).

* Corresponding author.

E-mail address: m.gholamikorzani@uq.edu.au (Maziar Gholami Korzani).

Peer review under responsibility of Hohai University.

http://dx.doi.org/10.1016/j.wse.2017.06.001

fluid motion in games (Gourlay, 2014; Nie et al., 2015). As a result, the qualitative visualization of fluid flow has almost always been the main concern, rather than the accuracy in fluid simulations in engineering applications. Takeda et al. (1994) simulated flow past a circular cylinder for Reynolds numbers less than 55, and their results perfectly matched the results from the finite difference method (FDM) and experimental data. Although they developed a no-slip boundary and a new viscosity equation, they carried out sensitivity analyses only on the smoothing length and domain shape. Morris et al. (1997) used SPH to simulate the same problem for very low Reynolds numbers ($Re \leq 1$). They proposed an artificial velocity for boundary particles to fulfill the no-slip boundary condition. They also used a simplified viscosity equation based on a finite difference approximation for very low Reynolds numbers. Marrone et al. (2013) obtained good results for the same problem using the δ-SPH method (Antoci et al., 2007). They also compared results for circular and square shapes with those obtained from FDM, and mostly studied the effects of obstacle shape and vortices geometries. Nonetheless, a series of questions, including selection of a smoothing function, smoothing length, and different viscosity equations, as well as impacts of background pressure and the speed of sound, have remained unsolved.

The capability of this method should be examined quantitatively in relation to a well-documented problem such as flow over a bluff body (Anderson, 2007), to provide an appropriate benchmark to verify the accuracy and validity of a numerical method as well as a newly developed code. In this study, a weakly compressible SPH method was adopted (Monaghan, 2005). The drag coefficient, as the main output, was studied for different SPH variables, including viscosity equations, kernels, smoothing lengths, speed of sound, and background pressures, as well as the domain parameters, including dimensions and resolution numbers. This study provides a practical approach to increasing the accuracy of future SPH simulations.

This paper is structured as follows: the SPH method is described in the subsequent section, the third section briefly explains the developed code, flow past a circular cylinder is discussed intensively in the fourth section, and the paper closes with a discussion of this work as well as planned extensions of it.

2. SPH method

The SPH method, originally developed for astrophysical purposes (Gingold and Monaghan, 1977; Lucy, 1977), is basically an interpolation technique. A comprehensive review of this method is presented in Liu and Liu (2005) and Monaghan (1994). In SPH, the computational domain is discretized into a finite number of particles (or integration points). These particles carry material properties such as velocity, density, and stress, and move with the material velocity according to the governing equations. The material properties of each particle are then calculated through the use of an interpolation process over its neighboring particles (integration domain) (Bui and Fukagawa, 2013). The interpolation process is based on the integral representation of a field function. Numerous scientists have recently shown interest in this method and introduced details on the derivation and formulation of SPH (Li and Liu, 2004; Liu and Liu, 2005, 2010). Below, the SPH method is introduced in detail against the background of this study. As is generally known, fluid motion is governed by the continuity and momentum (Navier-Stokes) equations, which are formulated in SPH as follows:

The continuity equation:

$$\frac{\mathrm{d}\rho_\mathrm{a}}{\mathrm{d}t} = \rho_\mathrm{a} \sum_\mathrm{b} \frac{m_\mathrm{b}}{\rho_\mathrm{b}} (\boldsymbol{v}_\mathrm{a} - \boldsymbol{v}_\mathrm{b}) \cdot \nabla_\mathrm{a} W_\mathrm{ab} \tag{1}$$

The momentum equation:

$$\frac{\mathrm{d}\boldsymbol{v}_\mathrm{a}}{\mathrm{d}t} = -\sum_\mathrm{b} m_\mathrm{b} \left(\frac{P_\mathrm{a}}{\rho_\mathrm{a}^2} + \frac{P_\mathrm{b}}{\rho_\mathrm{b}^2} \right) \nabla_\mathrm{a} W_\mathrm{ab} + \left\{ \frac{\mu}{\rho} \nabla^2 \boldsymbol{v} \right\}_\mathrm{a} \tag{2}$$

where t is time; W_ab is the kernel (smoothing function), which should have particular characteristics in order to approximate Dirac's delta function (Li and Liu, 2004); ∇_a denotes the gradient with respect to the coordinates of particle a; the subscripts a and b denote the integration point and particles in the neighborhood of particle a, respectively; and the particle field variables are $\boldsymbol{v}$, P, m, μ, and ρ, which represent the velocity, pressure, mass, dynamic viscosity, and density, respectively. The last term in the momentum equation denotes the viscosity, which will be discussed in Section 2.2.

2.1. Equation of state

In a weakly compressible SPH (WCSPH) method, an equation of state (EOS) must be used to correlate density and pressure. As shown in Eq. (2), the pressure plays an essential role, so the estimation of pressure from the density field is of paramount importance in the WCSPH method. Three options are available:

$$P = C_\mathrm{s}^2 \rho \tag{3}$$

$$P = C_\mathrm{s}^2 (\rho - \rho_0) \tag{4}$$

$$P = P_0 + C_\mathrm{s}^2 (\rho - \rho_0) \tag{5}$$

where C_s is the speed of sound and should be greater than $10U$, with U being the upstream velocity of the flow (Monaghan, 1988); and ρ_0 and P_0 are the density and background pressure at rest (initial condition), respectively.

EOS also has a significant effect on tensile instability, which is a well-documented issue in SPH, by maintaining a persistent positive pressure. SPH particles repel each other when the pressure is positive, similarly to atoms, and attract each other in the case of negative pressure, unlike atoms. However, the attraction causes SPH particles to form clumps, resulting in tensile instability (Monaghan, 2000; Swegle et al., 1995).

The ideal gas EOS (Eq. (3)) (Morris et al., 1997) avoids clustering of particles since it always maintains a positive pressure, but it requires very small time steps due to the possibility of localized high pressure. An alternative approach is to choose larger time steps in Eq. (4), which is computationally more efficient (Fang et al., 2006). However, Eq. (4) does suffer from particle clustering due to the development of negative pressure. For the flow past an obstacle, the pressure becomes negative in the wake of the bluff body. This problem can be overcome through introduction of the background pressure P_0 in Eq. (4) (Marrone et al., 2011, 2013; Morris, 1996). Consequently, Eq. (5) was chosen for this study in order to keep the pressure field positive and to avoid the tensile instability. It should be noted that the background pressure is only applicable to problems with a confined domain. In the case of a free surface problem, there is no need to use this term, since the gravity acceleration can almost always keep the pressure field positive. Alternatively, an artificial pressure (stress) should be used to deal with the tensile instability (Monaghan, 2000).

2.2. Viscosity equation

In SPH, the chosen viscosity not only determines the behavior of the liquid, but also influences the performance of the numerical calculation. Therefore, an artificial viscosity is often employed in SPH instead of the real viscosity component of the Navier-Stokes equation (the last term of Eq. (2)) (Gholami Korzani et al., 2016). The artificial viscosity was proposed by Monaghan and Gingold (1983) to dampen non-physical numerical oscillations and to simulate shock waves (Monaghan, 2012). Although this viscosity conserves total linear and angular momentum exactly, it is not a suitable approach to modeling viscous fluids. Therefore, an appropriate viscosity term, which should be properly adapted to the SPH scheme, is needed to simulate the shear flow more realistically. Several viscosity equations from the literature were used and are compared below:

(1) Morris et al. (1997):

$$\left\{\frac{\mu}{\rho}\nabla^2\boldsymbol{v}\right\}_{\mathrm{a}}=\sum_{\mathrm{b}}\frac{m_{\mathrm{b}}(\mu_{\mathrm{a}}+\mu_{\mathrm{b}})\boldsymbol{v}_{\mathrm{ab}}}{\rho_{\mathrm{a}}\rho_{\mathrm{b}}}\left(\frac{1}{r_{\mathrm{ab}}}\frac{\partial W}{\partial r_{\mathrm{a}}}\right) \tag{6}$$

where r_{ab} and $\boldsymbol{v}_{\mathrm{ab}}$ are the distance and velocity vector ($\boldsymbol{v}_{\mathrm{ab}}=\boldsymbol{v}_{\mathrm{a}}-\boldsymbol{v}_{\mathrm{b}}$) between particles a and b, respectively. $\partial W/\partial r_{\mathrm{a}}$ denotes the value of the derivative of the kernel function with respect to the location of particle a (r_{a}) for r_{ab}. This formulation conserves linear momentum exactly, while angular momentum is only approximately conserved.

(2) Shao and Lo (2003):

$$\left\{\frac{\mu}{\rho}\nabla^2\boldsymbol{v}\right\}_{\mathrm{a}}=\sum_{\mathrm{b}}\frac{4m_{\mathrm{b}}(\mu_{\mathrm{a}}+\mu_{\mathrm{b}})\boldsymbol{v}_{\mathrm{ab}}}{(\rho_{\mathrm{a}}+\rho_{\mathrm{b}})^2}\left(\frac{1}{r_{\mathrm{ab}}}\frac{\partial W}{\partial r_{\mathrm{a}}}\right) \tag{7}$$

Eq. (7) is a mixture of a standard SPH first derivative, with a finite difference approximation for the first derivative.

(3) Takeda et al. (1994):

$$\begin{aligned}\left\{\frac{\mu}{\rho}\nabla^2\boldsymbol{v}+\frac{1}{\rho}\left(\zeta+\frac{\mu}{3}\right)\nabla(\nabla\cdot\boldsymbol{v})\right\}_{\mathrm{a}}&=\sum_{\mathrm{b}}\frac{m_{\mathrm{b}}(\mu_{\mathrm{a}}+\mu_{\mathrm{b}})}{2\rho_{\mathrm{a}}\rho_{\mathrm{b}}}\\&\times\left[\boldsymbol{v}_{\mathrm{ab}}\left(n+\frac{1}{3}\right)\left(\frac{1}{r_{\mathrm{ab}}}\frac{\partial W}{\partial r_{\mathrm{a}}}\right)+\left(\frac{\boldsymbol{v}_{\mathrm{ab}}\cdot\boldsymbol{x}_{\mathrm{ab}}}{3}\boldsymbol{x}_{\mathrm{ab}}+r_{\mathrm{ab}}^2\boldsymbol{v}_{\mathrm{ab}}\right)\right.\\&\left.\times\frac{1}{r_{\mathrm{ab}}}\frac{\partial}{\partial r_{\mathrm{a}}}\left(\frac{1}{r_{\mathrm{ab}}}\frac{\partial W}{\partial r_{\mathrm{a}}}\right)\right]\end{aligned} \tag{8}$$

where n is the dimension of the problem, and $\boldsymbol{x}_{\mathrm{ab}}$ is the position vector, which is defined as $\boldsymbol{x}_{\mathrm{ab}}=\boldsymbol{x}_{\mathrm{a}}-\boldsymbol{x}_{\mathrm{b}}$. Although the solution of this equation employs the second derivative of the kernel, it is the exact derivation of viscosity from the Navier-Stokes equations. The most important assumption in Eq. (8) is that the fluid is compressible, and the bulk viscosity, ζ, can be considered negligible.

(4) Incompressible viscosity:

$$\begin{aligned}\left\{\frac{\mu}{\rho}\nabla^2\boldsymbol{v}\right\}_{\mathrm{a}}=\sum_{\mathrm{b}}\frac{m_{\mathrm{b}}(\mu_{\mathrm{a}}+\mu_{\mathrm{b}})}{2\rho_{\mathrm{a}}\rho_{\mathrm{b}}}&\left[n\boldsymbol{v}_{\mathrm{ab}}\left(\frac{1}{r_{\mathrm{ab}}}\frac{\partial W}{\partial r_{\mathrm{a}}}\right)+\right.\\&\left.r_{\mathrm{ab}}\boldsymbol{v}_{\mathrm{ab}}\frac{\partial}{\partial r_{\mathrm{a}}}\left(\frac{1}{r_{\mathrm{ab}}}\frac{\partial W}{\partial r_{\mathrm{a}}}\right)\right]\end{aligned} \tag{9}$$

This equation was used in this study as it considers the fluid incompressible by assuming the divergence term $(\nabla\cdot\boldsymbol{v})$ to be equal to zero.

2.3. Kernel

The smoothing function, also called the kernel, is of utmost importance since the performance of SPH critically depends on it. Kernels must satisfy numerous conditions, such as unity (the volume integral is equal to one), compact support (the kernel must not have an infinite reach), and positivity (Li and Liu, 2004). Kernels depend on the smoothing length, h, and a non-dimensional distance between particles, $q=r/h$. In this study, some well-known kernels were tested:

(1) Quadratic (Johnson et al., 1996):

$$W(r,h)=\alpha_{\mathrm{d}}\left(\frac{3}{16}q^2-\frac{3}{4}q+\frac{3}{4}\right)\quad 0\le q\le 2 \tag{10}$$

where α_{d} is $2/(\pi h^2)$ in two dimensions and $5/(4\pi h^3)$ in three dimensions. This kernel was used to simulate high-velocity impact problems. However, the second derivative of the kernel is a constant value, which is not suitable for Eqs. (8) and (9).

(2) Cubic spline (Monaghan, 1988):

$$W(r,h)=\begin{cases}\alpha_{\mathrm{d}}\left(1-\frac{3}{2}q^2+\frac{3}{4}q^3\right) & 0\le q\le 1\\ \frac{1}{4}\alpha_{\mathrm{d}}(2-q)^3 & 1\le q\le 2\\ 0 & q\ge 2\end{cases} \tag{11}$$

where α_d is $10/(7\pi h^2)$ in two dimensions and $1/(\pi h^3)$ in three dimensions. This kernel has been, so far, the most widely used kernel in SPH literature.

(3) Quintic (Wendland C2) (Wendland, 1995)

$$W(r,h)=\alpha_d\left(1-\frac{q}{2}\right)^4(2q+1)\quad 0\le q\le 2 \tag{12}$$

where α_d is $7/(4\pi h^2)$ in two dimensions and $7/(8\pi h^3)$ in three dimensions. In general, the higher the order of the kernel is, the greater the accuracy of the SPH scheme will be. Therefore, it provides the best compromise between accuracy and computational time.

(4) Quintic spline (Morris et al., 1997; Schoenberg, 1946):

$$W(r,h)=\begin{cases}\alpha_d\left[(3-q)^5-6(2-q)^5+15(1-q)^5\right] & 0\le q\le 1\\ \alpha_d\left[(3-q)^5-6(2-q)^5\right] & 1\le q\le 2\\ \alpha_d(3-q)^5 & 2\le q\le 3\\ 0 & q\ge 3\end{cases} \tag{13}$$

where α_d is $7/(47\pi h^2)$ in two dimensions and $1/(120\pi h^3)$ in three dimensions. This approach resembles a Gaussian kernel with a compact support. It is important to note that this kernel has a radius of influence of $3h$ and, therefore, more particles interact with one another, potentially reducing the computational efficiency.

Fig. 1 shows the calculated functions for the presented kernels and their first and second derivatives, as well as the Laplacian, as a function of q when $h=1$ and $n=2$. In addition, the impacts of the introduced kernels on the problem are further discussed in Section 4.2.1. Several theoretical and mathematical studies have been conducted on kernels to investigate their influences on SPH performance (Dehnen and Aly, 2012; Violeau and Leroy, 2014). As a result, the kernel standard deviation is the most important parameter in comparing distinct kernels. However, the aim of the present study was to practically investigate the effects of the chosen kernel on the result of the calculations.

2.4. Boundary conditions

2.4.1. Solid boundary

Immovable solid bodies are usually built with parallel layers of fluid particles fixed in place but not allowed to move, and thus acting as a solid boundary (Dalrymple and Knio, 2001). In other words, Eq. (2) is calculated for each boundary particle, but the location and velocity of each particle are not updated at the end of each time step. Nevertheless, forces acting on the solid body can be obtained by summing Eq. (2) over all fixed boundary particles multiplied by their masses. The most significant advantage of this approach is that the computational treatment of the system is considerably simplified, since no special considerations are necessary for boundary particles, except for the constraint of no movement. Several layers of particles are needed to avoid the kernel support domain truncation, since the truncation produces some errors in estimating the key variables, such as the density.

The essential characteristic of a solid boundary is the enforcement of the no-slip condition. Morris et al. (1997) used an antisymmetric approximation method, which was similar to that of Takeda et al. (1994), to extrapolate the velocity of free particles through fixed boundary particles. In simple terms, the fixed boundary particles have an artificial velocity that mirrors their free particle counterparts to ensure that the overall fluid velocity on the surface is zero.

2.4.2. Inflow/outflow boundary

The inflow/outflow algorithm proposed by Federico et al. (2012) was used to generate steady continuous flow. As shown in Fig. 2, two new sets of boundary particles (inflow and outflow particles) are defined at the domain boundaries in order to impose distinct upstream and downstream flow conditions. The inflow/outflow particles affect the free fluid particles within the domain. The inverse is not true, as the inflow/outflow particles are unaffected by the free ones. The inflow/outflow region covered by these particles must be at least as wide as the kernel domain.

At the inflow boundary, the desired velocity and density are assigned to the inflow particles. They are distributed on a regular grid and move according to their assigned velocity. When an inflow particle crosses the inflow threshold, it becomes a free fluid particle and will move according to the governing equations. At the outflow boundary, it is possible to impose specific outflow conditions similar to the inflow condition. Nonetheless, a fluid particle that crosses the outflow threshold becomes an outflow particle and all its field variables are maintained constant with time, except for the location, which evolves according to its velocity. Further details of the computational procedure are reported in Federico et al. (2012).

2.4.3. Periodic boundary

For this type of boundary condition, the cubical simulation box is replicated throughout space to form an infinite lattice, which is often used to eliminate surface effects from the computation. This boundary condition was applied perpendicular to the flow direction (Fig. 2) and implemented by considering that particles located at a boundary are linked to particles at the opposite boundary. Therefore, a particle that leaves a boundary immediately re-enters at the opposite boundary with the same velocity.

3. Programming

An open source code, called PersianSPH (Gholami Korzani et al., 2015), has been developed in C++ to solve the introduced equations. All calculations and neighbor searching were conducted in parallel using the OpenMP library. Therefore, the whole domain was divided into several segments, and then the cell-linked list approach (Hockney and Eastwood, 1988) was

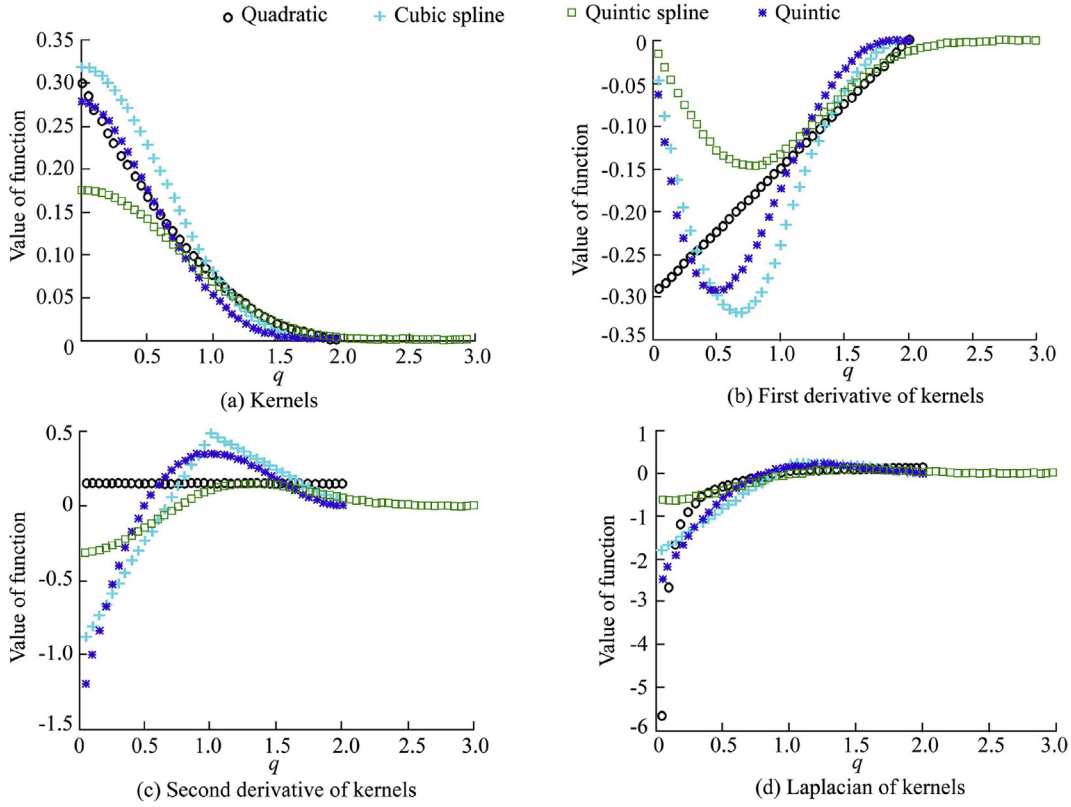

Fig. 1. Comparison of kernels and derivative values for $h = 1$ and $n = 2$.

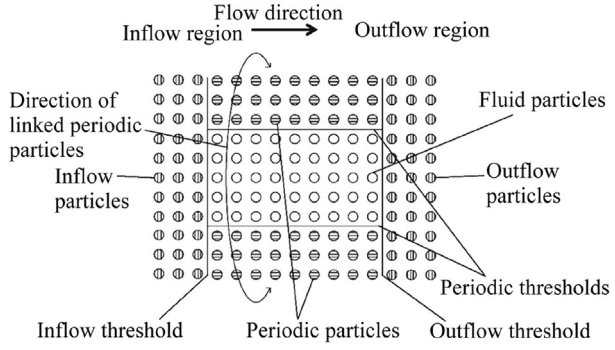

Fig. 2. Initial sketch of boundary conditions.

used to find neighboring particles in order to calculate the forces between them in parallel. There is no particular limitation to the number of particles, unless the number of threads is restricted. In addition, the modified Verlet scheme (Monaghan, 1994) was used for time integration. The time step size, Δt, of the integration method used has to be limited for stability reasons based on several criteria, which can be summarized as follows:

Courant-Friedrichs-Lewy (CFL) condition:

$$\Delta t \leq 0.25\min(h/C_s) \tag{14}$$

Condition on the viscous diffusion:

$$\Delta t \leq 0.125\min\left(h^2/\nu\right) \tag{15}$$

Condition on the force per unit mass:

$$\Delta t \leq 0.25\min\sqrt{h/a_i} \tag{16}$$

where a_i is the acceleration of particle i, and ν denotes the fluid kinematic viscosity. The chosen time step size must be smaller than the minimum of these conditions.

4. Flow past a circular cylinder

4.1. Modeling case

The main problem studied was the calculation of the drag coefficient for a two-dimensional (2D) circular cylinder under the influence of various SPH parameters. As shown in Fig. 3, the periodic boundary was used in the vertical direction, and the inflow/outflow boundaries were used to generate a steady flow in the horizontal direction. A solid boundary was used to simulate the circular cylinder.

Parameters studied can be divided into two main categories: SPH factors such as kernel choices, and domain factors such as the domain shape. All parameters and coefficients will be introduced and discussed thoroughly in Section 4.2. However, all the parameters considered are defined concisely in Section 2 and Fig. 3, except for the resolution number, which is the ratio of the cylinder diameter to the initial distance between SPH particles at time zero (refer to Section 4.2.7).

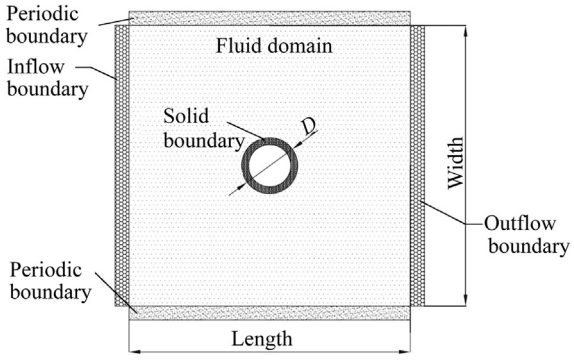

Fig. 3. Schematic view of domain and boundaries.

4.2. Numerical results

As described earlier, the primary goal of this study was to achieve accurate results for the drag coefficient, which can be compared with experimental data. To achieve the best result, several modifications are required from a base setup of input parameters defining the numerical model. Inevitably, some initial assumptions made to simulate the problem must be used for the investigated parameters at early stages. Afterwards, an appropriate value or equation is chosen to replace the initial assumptions based on the results of each modification stage. By modifying these parameters step by step, the drag coefficient, as the main output of this study, gradually converges to the experimental value. Finally, the drag coefficient is calculated for numerous Reynolds numbers based on the modified and calibrated models.

For the initial calculations in this study, the Reynolds number was fixed at 60 for all stages, unless otherwise noted. The target drag coefficient C_d, extracted from the available experimental data (Anderson, 2007), was 1.41 for this Reynolds number. A square with side lengths eight times the cylinder diameter was modeled as the whole domain, and the cylinder was located in the middle. In addition, the smoothing length, the speed of sound, and background pressure were 1.1 times the initial distance of particles, ten times the imposed flow speed, and $0.07C_s^2\rho_0$, respectively. The resolution number was 30, and the Morris viscosity equation (Eq. (6)) was employed. The impacts of these factors and selection criteria will be discussed in Sections 4.2.1 through 4.2.7.

4.2.1. Kernel selection

Various kernels have been introduced in Section 2.3. As shown in Fig. 1, there are significant differences between the kernels and their derivatives, so it seems obvious that the results for different kernels must be very different as well. However, it should be noted that the optimum smoothing lengths for each kernel are not identical. Therefore, a fair comparison of kernels requires the selection of the individual optimum smoothing length.

Simulations for each kernel were conducted using the properties introduced in Section 4.2. The smoothing length was not changed, so the number of neighboring particles was maintained constant, except for the case of the quintic spline kernel. As shown in Fig. 4, the quintic spline is the most suitable kernel, with $C_d = 1.79$, because this kernel shows the best match with the experimental results and its C_d time history curve is smoother (without any fluctuations) than that of the other kernels in the steady state condition. Although this kernel is computationally less efficient, it is the most reliable kernel for the problem considered. Therefore, the quintic spline kernel was used for the rest of the study. The accuracy of results using this kernel has been investigated by Gholami Korzani et al. (2014).

4.2.2. Smoothing length

After choosing a proper kernel, finding the optimum smoothing length, h, is the next critical step. The number of neighboring particles grows significantly with increasing h, which decreases the computational efficiency. In SPH, the smoothing length is dependent on particle packing and the initial distance between particles. Hence, the problem was studied with various smoothing lengths. The smoothing length equals $\alpha\Delta x$, where Δx is the initial distance between particles at the initial time step, and α varied from 0.9 to 1.3.

As shown in Fig. 5, the simulations for $\alpha = 0.9$ and 1.0 ended earlier since they were highly unstable. The values of drag coefficient C_d for α values of 0.9, 1.0, 1.1, 1.2, and 1.3 were 1.46, 1.59, 1.79, 1.79, and 1.79, respectively. C_d was exactly the same for α values of 1.1, 1.2, and 1.3, demonstrating that a state had been reached in which the smoothing length did not change the results. Since the computation time increased with increasing h, the optimal value for α was 1.1, which was maintained for the rest of the study. It is worth noting that although this optimum value results in a C_d value that is quite different from the experimental value of 1.41, the difference can be reduced further with the introduction of other modifications.

4.2.3. Viscosity equation

As already explained in Section 2.2, all equations for modeling the viscosity effect have advantages and disadvantages. Four simulations were conducted to determine the impacts of these equations on the resulting values of C_d. The drag force is usually divided into two components: frictional drag and pressure drag. Frictional drag is derived from the friction between the fluid and the surface and involves viscous flow.

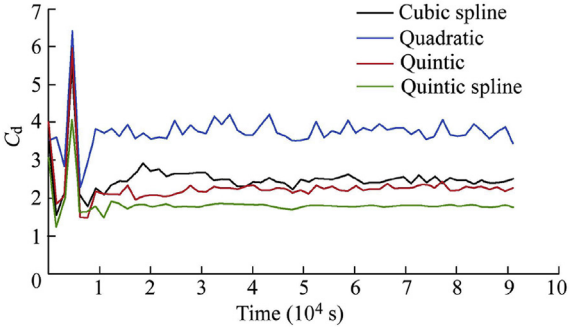

Fig. 4. Drag coefficient curve vs. time for different kernels.

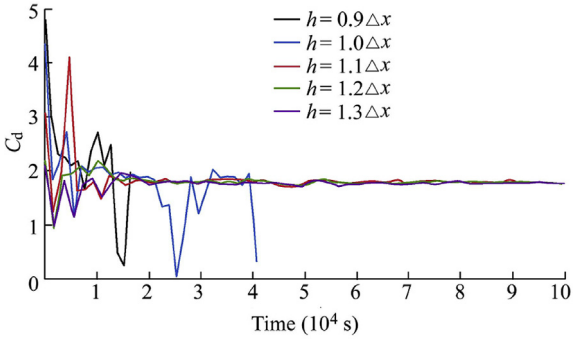

Fig. 5. Drag coefficient curve vs. time for various smoothing lengths.

Pressure drag is derived from eddying motions and is associated with the formation of a wake. The viscous drag force also individually shows the effect of the viscosity equation. Hence, two coefficients were calculated: the total and viscous drag coefficients. They are compared for the different equations used in Table 1.

As illustrated in Fig. 6 and Table 1, there is no significant difference between the resulting drag coefficients. However, some discrepancies were observed in the transient state condition, showing that the results of Eqs. (8) and (9) were slightly smoother. Eqs. (6) and (7) were proposed for low Reynolds numbers. Since the results for the equation of Takeda et al. (Eq. (8)) and the equation of incompressible viscosity (Eq. (9)) were closer to the experimental value of C_d, Eq. (8) was chosen for later simulations. There was no difficulty in obtaining the second derivative of the kernel, which is needed for the application of the viscosity equation of Takeda et al. (1994), because the quintic spline kernel as a high-order kernel was used.

Table 1
Drag coefficients for different viscosity equations.

Equation	Total C_d	Viscous C_d
Morris et al. (1997) (Eq. (6))	1.79	0.52
Shao and Lo (2003) (Eq. (7))	1.80	0.52
Takeda et al. (1994) (Eq. (8))	1.73	0.50
Incompressible viscosity (Eq. (9))	1.73	0.50

4.2.4. Background pressure

As already discussed in Section 2.1, the value for the background pressure, P_0, should be defined in such a way that no negative pressure is generated during simulations. In order to explore this, P_0 can be defined as $\beta C_s \rho_0$, where β is a coefficient used to adjust P_0. Consequently, P_0 will become zero if β approaches zero (i.e., no background pressure). Conversely, the EOS will be transformed into that of the ideal gas if β approaches unity. Fig. 7 illustrates the fluctuations of C_d with increasing β, but in all cases it reached the same steady state value for C_d. This study attempted to maintain β as low as possible to minimize fluctuations and maintain a positive pressure. A value of $\beta = 0.07$ was chosen for the remainder of the study.

4.2.5. Speed of sound

The speed of sound in the fluid, C_s, as another important component of the EOS, influences the selection of the time step and resulting density fluctuations. With the increase of the speed of sound, the time step must be reduced, and the density variations become negligible. In contrast, density variations will be increased by reducing the speed of sound, which means that the fluid displays a higher compressibility. Therefore, a balance should be established between the time step and weak compressibility by optimizing the speed of sound in the fluid.

The speed of sound in the fluid is proportional to the fluid velocity U, leading to $C_s = \lambda U$. This is an appropriate approach since the idea is not to use realistic values for the speed of sound, but to keep the Mach number U/C_s small and to reduce compressibility effects. In this study, λ varied from 5 to 20. Fig. 8 shows that all curves reached a particular convergence value, but those with higher values for the speed of sound had greater fluctuations in the transient state. As a result, the speed of sound was chosen to be ten times the fluid velocity as suggested by Monaghan (1988).

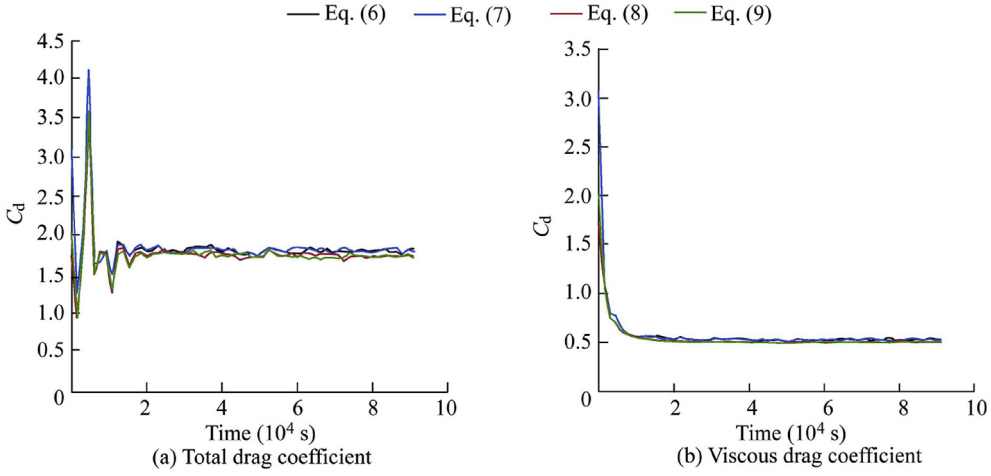

Fig. 6. Drag coefficient curve vs. time for various viscosity equations.

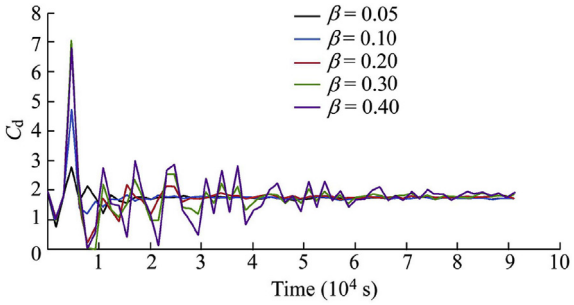

Fig. 7. Drag coefficient curve vs. time for various background pressures.

4.2.6. Problem domain geometrical shape

Two geometrical shapes were considered in this study to model the whole domain of the problem: a square ($L = W$, where L is the length and W is the width), and a rectangle ($L = 2W$) (Fig. 3). Six different side lengths, proportional to the diameter of the cylinder, were investigated for the square domain shape. As demonstrated in Fig. 9, the drag coefficient decreased gradually with increasing side length, and finally reached a plateau, signaling the point when the results were independent of the domain size. Table 2 shows the drag coefficient and relative difference between the calculated and experimental (1.41) drag coefficients, and also shows that the square domain shape resulted in an accurate drag coefficient. Since the number of particles grows significantly with increasing side length of the problem domain, it may be preferable to reach a compromise in accuracy by reducing the domain size. Although the obtained C_d value for the square with a side length greater than $20D$ is closer to the experimental value, it is not computationally beneficial. Hence, to establish a balance between accuracy and computational time, the C_d value can be in an acceptable range for a square with a side length of $16D$.

On the other hand, a rectangular domain shape is advantageous, since the number of particles is reduced to half that of the square domain shape. To study the impact of the rectangular domain on the accuracy of the results, two different flow velocities were considered. The results show that the drag coefficient values for Reynolds numbers of 60 and 200 were 1.48 and 1.26, respectively, for the square domain, and 1.58 and 1.32, respectively, for the rectangular domain. Therefore,

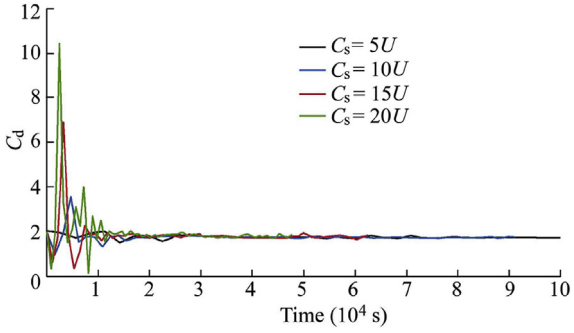

Fig. 8. Drag coefficient curve vs. time for various speeds of sound.

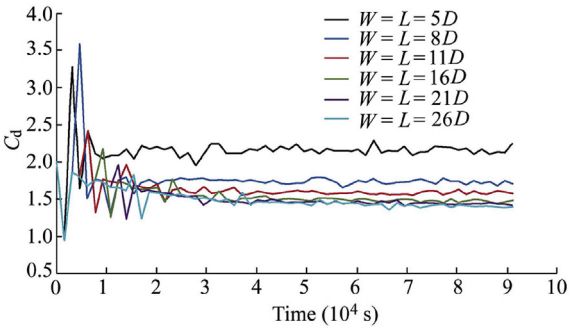

Fig. 9. Drag coefficient curve vs. time for square domain shape with various side lengths.

Table 2
Drag coefficient for square domain shape with various side lengths.

Side length	C_d	Relative difference (%)	Side length	C_d	Relative difference (%)
$5D$	2.16	53.2	$16D$	1.48	5.0
$8D$	1.73	22.7	$21D$	1.45	2.8
$11D$	1.59	12.8	$26D$	1.42	0.7

the discrepancies between the drag coefficients calculated for the square and rectangular domain shapes were less than 7% and 4% for Reynolds numbers of 60 and 200, respectively. The difference between the rectangular domain shape results and experimental data was around 13% for both flow conditions.

In addition, under the rectangular domain shape, a shifted cylinder condition was studied. In this condition, the cylinder was shifted about $5.5D$ to the left. Consequently, the calculated drag coefficient (for a Reynolds number of 200) was 1.49, which was 13% greater than that calculated for the centered cylinder. Thus, the best condition for both domain shapes is the centered cylinder.

The results for the square domain shape were more accurate than those for the rectangular domain shape. However, the rectangular domain shape is preferred for reducing the computational time. Accordingly, the square domain shape was used for Reynolds numbers less than and equal to 200, since these simulations were not computationally demanding. In contrast, the rectangular domain shape was selected for $Re = 500$. As will be seen later, even with the rectangular domain shape, the results are accurate enough compared with the experimental data.

4.2.7. Resolution number (spatial resolution)

As stated previously, the resolution number, $D/\Delta x$, is defined as the ratio of the cylinder diameter to the initial distance between particles. To demonstrate how this factor affected the results, some simulations were carried out through variation of this number. Two different flow velocities (corresponding to Reynolds numbers of 60 and 200) were investigated and the resolution number varied from 10 to 80. It should be noted that the case of $Re = 60$ is a flow condition preceding the generation of vortices, and the case of $Re = 200$ is a flow condition following the generation of vortices in the wake of the cylinder.

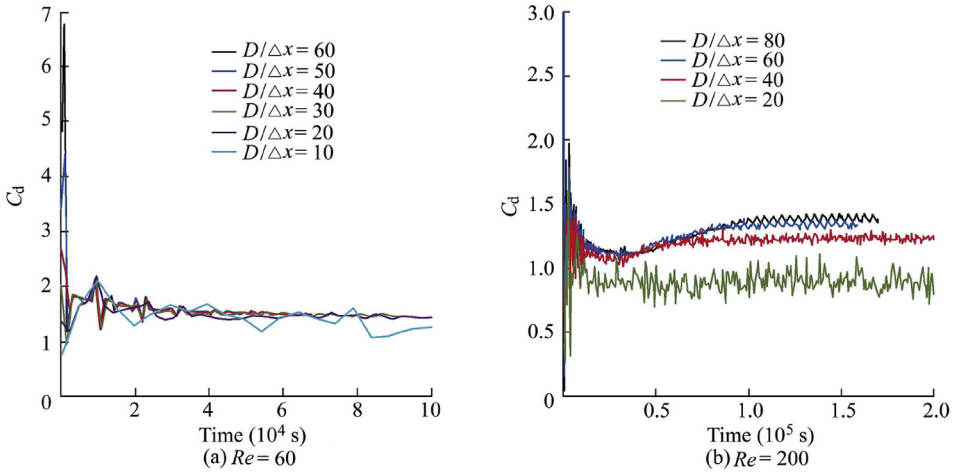

Fig. 10. Drag coefficient curve vs. time for various resolution numbers.

Fig. 10(a) illustrates that lower resolution numbers produced some noise in the results prior to the generation of vortices. In contrast, the drag coefficient rose gently to reach a plateau after the generation of vortices, as illustrated in Fig. 10(b). Therefore, the drag coefficient was strongly dependent on this factor, while this dependency was more significant for higher Reynolds numbers. A general result of this study is the observation that the resolution number is dependent on the Reynolds number. Fig. 10 shows that the drag coefficient is free and independent of the resolution number when the resolution number is greater than a certain value (e.g., 20 for $Re = 60$ and 60 for $Re = 200$). That means the value of the resolution number showing no influence on the drag coefficient must be determined manually for every Reynolds number, and is henceforth denoted as the optimum resolution number.

4.2.8. Reynolds number

Finally, the model calibrated using the above-mentioned seven steps (Sections 4.2.1 to 4.2.7) was used to study the dependency of the drag coefficient on the Reynolds number. In this section, results obtained from SPH were compared to available experimental data (Anderson, 2007).

Fig. 11 shows a comparison between the results of this study, the results of Marrone et al. (2013), and the available experimental data. Although there were some discrepancies between the acquired numerical results and the experimental data for Reynolds numbers exceeding 200, a satisfying agreement with experimental results was achieved. The deviation of the calculations from experimental results can be explained by the chosen rectangular domain shape and the smaller domain size (refer to Section 4.2.6).

Fig. 12 shows the velocity field on the left-hand side and velocity vectors on the right-hand side, around the cylinder for different Reynolds numbers, demonstrating agreement with experimental observations and previous studies (Marrone et al., 2013). In addition, Table 3 shows the minimum required resolution numbers for each *Re* value examined in this study, demonstrating that the drag coefficient is independent of the particle size. It is important to note that the maximum resolution number ($D/\Delta x = 80$) will work for every *Re* value considered in this study, and the choice of the individual values was made based on computational efficiency issues only.

5. Conclusions

The paper presents a comprehensive parametric study of the flow past a circular cylinder in two dimensions. The impacts of several SPH variables on the calculation of drag coefficients in the 2D problem were studied for Reynolds numbers ranging from 1 to 500. Through comparison with existing experimental data and results from other numerical tools, the results of this study showed strong agreement with the existing experimental data.

The significance of the studied parameters can be summarized as follows:

(1) The quintic spline kernel was the most reliable kernel for this study, even though it was computationally less efficient.

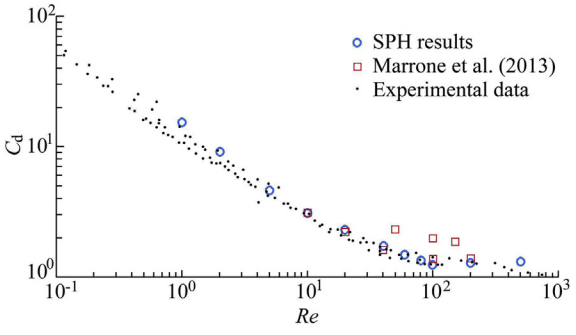

Fig. 11. Drag coefficient curve vs. Reynolds numbers for a circular cylinder obstacle.

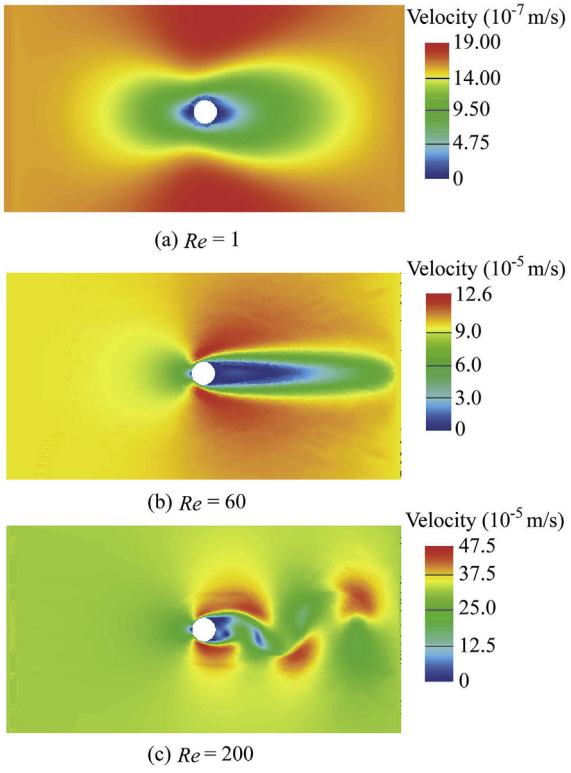

Fig. 12. Snapshots from velocity field (left) and corresponding velocity vectors (right) for different Reynolds numbers.

(2) Different viscosity equations did not have any noticeable impacts on the results. Therefore, the simplest equation (Eq. (6)) can be used to improve the computational efficiency. It should be noted that Eqs. (8) and (9) are beneficial for reproducing vortices as in the present study no turbulence model was adopted.

(3) The background pressure played a vital role in avoiding the clustering of particles due to tensile instability, but its drawback was some numerical noise in the results. Therefore, it must be maintained as low as possible to keep the pressure positive.

(4) Variation of the speed of sound did not affect the steady state results. It only produced fluctuations in the transient condition.

(5) The square shape of the problem domain was more accurate than the rectangular shape. However, the rectangular domain shape was preferred for higher Reynolds numbers to reduce the computational time without significantly compromising the accuracy.

(6) The most suitable side length for the square domain shape was 26D, but a square with a side length of 16D was used to establish a balance between the accuracy and the computational time.

(7) As SPH is computationally expensive, it is important to keep the model size as small as possible. Therefore, obtaining efficient problem domain sizes or shapes, and using proper boundary conditions (e.g., the periodic boundary condition) are absolutely important.

(8) The best location of the obstacle for achievement of the most accurate results was in the center of both considered domain shapes.

(9) The results were significantly sensitive to the resolution number for different flow velocities. Therefore, the resolution number was individually optimized for each Reynolds number in order to reach a threshold independent of particle size. This was done to reduce simulation time, but it is clear that the highest used resolution number will cover the complete range of Reynolds numbers considered in this study.

In conclusion, the presented results and discussion provide guidance and indications for the selection of parameters used to optimize numerical studies using SPH.

Table 3
Resolution number for each Reynolds number.

Re	$D/\Delta x$	Re	$D/\Delta x$	Re	$D/\Delta x$	Re	$D/\Delta x$
1	20	10	20	60	30	200	60
2	20	20	30	80	30	500	80
5	20	40	30	100	30		

References

Anderson, J.D., 2007. Fundamentals of Aerodynamics, fourth ed. McGraw-Hill Higher Education, Boston.

Antoci, C., Gallati, M., Sibilla, S., 2007. Numerical simulation of fluid-structure interaction by SPH. Comput. Struct. 85(11), 879−890. http://dx.doi.org/10.1016/j.compstruc.2007.01.002.

Bui, H.H., Sako, K., Fukagawa, R., 2007. Numerical simulation of soil-water interaction using Smoothed Particle Hydrodynamics (SPH) method. J. Terramech. 44(5), 339−346. http://dx.doi.org/10.1016/j.jterra.2007.10.003.

Bui, H.H., Fukagawa, R., 2013. An improved SPH method for saturated soils and its application to investigate the mechanisms of embankment failure: Case of hydrostatic pore-water pressure. Int. J. Numer. Anal. Methods Geomech. 37(1), 31−50. http://dx.doi.org/10.1002/nag.1084.

Dalrymple, R.A., Knio, O., 2001. SPH modelling of water waves. In: Proceedings of the Fourth Conference on Coastal Dynamics. ASCE, Lund Sweden.

Dehnen, W., Aly, H., 2012. Improving convergence in Smoothed Particle Hydrodynamics simulations without pairing instability. Mon. Notices R. Astronom. Soc. 425(2), 1068−1082. http://dx.doi.org/10.1111/j.1365-2966.2012.21439.x.

Fang, J., Owens, R.G., Tacher, L., Parriaux, A., 2006. A numerical study of the SPH method for simulating transient viscoelastic free surface flows. J. Newt. Fluid Mech. 139(1), 68−84. http://dx.doi.org/10.1016/j.jnnfm.2006.07.004.

Federico, I., Marrone, S., Colagrossi, A., Aristodemo, F., Antuono, M., 2012. Simulating 2D open-channel flows through an SPH model. Eur. J. Mech. B/Fluids 34, 35−46. http://dx.doi.org/10.1016/j.euromechflu.2012.02.002.

Gholami Korzani, M., Galindo-Torres, S.A., Williams, D., Scheuermann, A., 2014. Numerical simulation of tank discharge using Smoothed Particle Hydrodynamics. Appl. Mech. Mater. 553, 168−173. http://dx.doi.org/10.4028/www.scientific.net/AMM.553.168.

Gholami Korzani, M., Galindo-Torres, S.A., Scheuermann, A., 2015. PersianSPH: A Multi-physical Smoothed Particle Hydrodynamics Code. http://korzani.wixsite.com/persiansph/persiansph [Retrieved 29 October 2016].

Gholami Korzani, M., Galindo-Torres, S.A., Scheuermann, A., Williams, D., 2016. Smoothed Particle Hydrodynamics into the fluid dynamics of classical problems. Appl. Mech. Mater. 846, 73−78. http://dx.doi.org/10.4028/www.scientific.net/AMM.846.73.

Gingold, R.A., Monaghan, J.J., 1977. Smoothed particle hydrodynamics: Theory and application to non-spherical stars. Mon. Notices R. Astronom. Soc. 181(3), 375−389. http://dx.doi.org/10.1093/mnras/181.3.375.

Gourlay, M.J., 2014. Fluid Simulation for Video Games. https://software.intel.com/en-us/articles/fluid-simulation-for-video-games-part-1 [Retrieved 29 October 2016].

Gray, J.P., Monaghan, J.J., Swift, R.P., 2001. SPH elastic dynamics. Comput. Methods Appl. Mech. Eng. 190(49), 6641−6662. http://dx.doi.org/10.1016/S0045-7825(01)00254-7.

Hockney, R.W., Eastwood, J.W., 1988. Computer Simulation Using Particles. CRC Press, Bristol.

Johnson, G.R., Stryk, R.A., Beissel, S.R., 1996. SPH for high velocity impact computations. Comput. Methods Appl. Mech. Eng. 139(1), 347−373. http://dx.doi.org/10.1016/S0045-7825(96)01089-4.

Li, S., Liu, W.K., 2004. Meshfree Particle Methods. Springer-Verlag, Berlin.

Liu, G.R., Liu, M.B., 2005. Smoothed Particle Hydrodynamics: A Meshfree Particle Method. World Scientific, New Jersey.

Liu, M.B., Liu, G.R., 2010. Smoothed Particle Hydrodynamics (SPH): An overview and recent developments. Archives Comput. Methods Eng. 17(1), 25−76. http://dx.doi.org/10.1007/s11831-010-9040-7.

Lucy, L.B., 1977. A numerical approach to the testing of the fission hypothesis. Astronom. J. 82, 1013−1024.

Marrone, S., Antuono, M., Colagrossi, A., Colicchio, G., Le Touzé, D., Graziani, G., 2011. δ-SPH model for simulating violent impact flows. Comput. Methods Appl. Mech. Eng. 200(13), 1526−1542. http://dx.doi.org/10.1016/j.cma.2010.12.016.

Marrone, S., Colagrossi, A., Antuono, M., Colicchio, G., Graziani, G., 2013. An accurate SPH modeling of viscous flows around bodies at low and moderate Reynolds numbers. J. Comput. Phys. 245, 456−475. http://dx.doi.org/10.1016/j.jcp.2013.03.011.

Mirmohammadi, A., Ketabdari, M.J., 2011. Numerical simulation of wave scouring beneath marine pipeline using Smoothed Particle Hydrodynamics. Int. J. Sediment Res. 26(3), 331−342. http://dx.doi.org/10.1016/S1001-6279(11)60097-8.

Monaghan, J.J., Gingold, R.A., 1983. Shock simulation by the particle method SPH. J. Comput. Phys. 52(2), 374−389. http://dx.doi.org/10.1016/0021-9991(83)90036-0.

Monaghan, J.J., 1988. An introduction to SPH. Comput. Phys. Commun. 48(1), 89−96. http://dx.doi.org/10.1016/0010-4655(88)90026-4.

Monaghan, J.J., 1994. Simulating free surface flows with SPH. J. Comput. Phys. 110(2), 399−406. http://dx.doi.org/10.1006/jcph.1994.1034.

Monaghan, J.J., 2000. SPH without a tensile instability. J. Comput. Phys. 159(2), 290−311. http://dx.doi.org/10.1006/jcph.2000.6439.

Monaghan, J.J., 2005. Smoothed particle hydrodynamics. Rep. Prog. Phys. 68(8), 1703−1759. http://dx.doi.org/10.1088/0034-4885/68/8/R01.

Monaghan, J.J., 2012. Smoothed particle hydrodynamics and its diverse applications. Annu. Rev. Fluid Mech. 44, 323−346. http://dx.doi.org/10.1146/annurev-fluid-120710-101220.

Morris, J., 1996. Analysis of Smoothed Particle Hydrodynamics with Applications. Ph. D. Dissertation. Monash University, Melbourne.

Morris, J., Fox, P., Zhu, Y., 1997. Modeling low Reynolds number incompressible flows using SPH. J. Comput. Phys. 136(1), 214−226. http://dx.doi.org/10.1006/jcph.1997.5776.

Nie, X., Chen, L., Xiang, T., 2015. Real-time incompressible fluid simulation on the GPU. Int. J. Comput. Games Technol. http://dx.doi.org/10.1155/2015/417417.

Schoenberg, I.J., 1946. Contributions to the problem of approximation of equidistant data by analytic functions, Part B: On the problem of osculatory interpolation, a second class of analytic approximation formulae. Q. Appl. Math. 4(2), 112−141.

Shao, S., Lo, E.Y.M., 2003. Incompressible SPH method for simulating Newtonian and non-Newtonian flows with a free surface. Adv. Water Resour. 26(7), 787−800. http://dx.doi.org/10.1016/S0309-1708(03)00030-7.

Swegle, J.W., Hicks, D.L., Attaway, S.W., 1995. Smoothed particle hydrodynamics stability analysis. J. Comput. Phys. 116(1), 123−134. http://dx.doi.org/10.1006/jcph.1995.1010.

Takeda, H., Miyama, S.M., Sekiya, M., 1994. Numerical simulation of viscous flow by smoothed particle hydrodynamics. Prog. Theor. Phys. 92(5), 939−960.

Violeau, D., Leroy, A., 2014. On the maximum time step in weakly compressible SPH. J. Comput. Phys. 256, 388−415. http://dx.doi.org/10.1016/j.jcp.2013.09.001.

Wendland, H., 1995. Piecewise polynomial, positive definite and compactly supported radial functions of minimal degree. Adv. Comput. Math. 4(1), 389−396. http://dx.doi.org/10.1007/BF02123482.